Article

High-Temperature Thermodynamics of Uranium from Ab Initio Modeling

Per Söderlind *[iD], Alexander Landa [iD], Emily E. Moore [iD], Aurélien Perron [iD], John Roehling and Joseph T. McKeown

Lawrence Livermore National Laboratory, Livermore, CA 94551-0808, USA
* Correspondence: soderlind@llnl.gov; Tel.: +1-925-423-4667

Abstract: We present high-temperature thermodynamic properties for uranium in its γ phase (γ-U) from first-principles, relativistic, and anharmonic theory. The results are compared to CALPHAD modeling. The ab initio electronic structure is obtained from density-functional theory (DFT) that includes spin–orbit coupling and an added self-consistent orbital-polarization (OP) mechanism for more accurate treatment of magnetism. The first-principles method is coupled to a lattice dynamics scheme that is used to model anharmonic lattice vibrations, namely, Self-Consistent Ab Initio Lattice Dynamics (SCAILD). The methodology can be summarized in the acronym DFT + OP + SCAILD. Upon thermal expansion, γ-U develops non-negligible magnetic moments that are included for the first time in thermodynamic theory. The all-electron DFT approach is shown to model γ-U better than the commonly used pseudopotential method. In addition to CALPHAD, DFT + OP + SCAILD thermodynamic properties are compared with other ab initio and semiempirical modeling and experiments. Our first-principles approach produces Gibbs free energy that is essentially identical to CALPHAD. The DFT + OP + SCAILD heat capacity is close to CALPHAD and most experimental data and is predicted to have a significant thermal dependence due to the electronic contribution.

Keywords: uranium; specific heat; anharmonic; first principles; CALPHAD; DFT

1. Introduction

Uranium metal is recognized as a nuclear fuel for sodium fast reactors due to its significant thermal conductivity, high fissile material density, high burnup capability, inherent ability to incorporate minor actinides, and excellent neutron economy relative to mixed oxide fuels (MOX) [1–7]. However, metallic uranium-based nuclear fuels undergo physical phenomena that are poorly understood on a fundamental level. These phenomena include gaseous swelling, redistribution of constituents, or phase separation as consequences of the fabrication procedures. α-U and γ-U allotropes as well as liquid uranium are all states of great interest because they are involved in the technological processes of nuclear fuel operation. In addition, the thermophysical properties of γ-uranium are not only important for the operation of nuclear reactors but also for the relevant fuel-fabrication mechanics such as casting, rolling, and forming. These processes can be modeled but casting-solidification predictions are particularly sensitive to the thermophysical properties such as heat capacity. There is a remarkable scatter in the experimentally derived heat capacities for γ-uranium, as we shall illustrate below, but reliable thermodynamic data and higher confidence in the properties immediately following solidification are needed to improve model predictions.

Uranium has three solid phases (crystal structures) at ambient pressure: the face-centered orthorhombic α-U, the tetragonal β-U, and the high-temperature body-centered cubic (bcc) γ-U. At temperature $T = 942.02$ K and ambient pressure, α-U transforms to β-U. At $T = 1048.99$ K, β-U transforms to γ-U, then at $T = 1407.99$ K, γ-U melts, and the liquid to vapor transformation of uranium metal occurs at $T = 4432.08$ K [8]. The α phase has unique anisotropic properties, anisotropic thermal expansion that is probably related to the

anisotropic growth during irradiation, and along with susceptibility of α-U to corrosion by water, prompted the choice of the MOX rather than metal form of uranium as a fuel for commercial light water reactors [6,7]. Most of the experimental work has been performed on the α phase and not on the γ phase because of the mechanical and dynamical instability of the latter at room temperature [9]. Performing high-temperature experiments on nuclear materials poses significant challenges that ultimately limit experimental investigations of the γ phase [6–8].

Uranium is also a fascinating metal from a fundamental and academic standpoint. The electronic structure dominates by narrow 5f bands that tend to break crystal symmetry and bond the atoms in a complex and distorted fashion [9–15]. The mechanism that stabilizes the open and complex structures in systems with narrow bands can be described in terms of a Peierls or Jahn–Teller distortion [9,12]: a system with narrow bands close to the Fermi level can gain energy by lowering the crystal-structure symmetry. This phenomenon explains the low-symmetry orthorhombic structure of α-uranium as well as the complex structures of the light actinides Pa–Pu. Higher symmetry allotropes, such as γ-U, are dynamically unstable at low temperatures due to the Peierls crystal symmetry-breaking mechanism. At higher temperatures, however, γ-U is dynamically stabilized and favored over α-U due to entropy of thermal atomic vibrations [13], analogous to the temperature-driven formation of the body-centered cubic phase in the hexagonal elements Ti, Zr, and Hf, for example.

Numerous first-principles calculations have been performed to evaluate uranium's structural, mechanical, and thermal properties, as well as radiation damage (defects). The stability of uranium and its alloys has been explored using different methods founded on density-functional theory (DFT) [9–66]. These methods include the all-electron full-potential linear muffin-tin orbitals (FPLMTO) method [9–16,27,53,60,64,65] and the plane-wave-based projector augmented wave (PAW) method that utilizes the pseudopotential approximation [17–26,32,37,39,45,46,52,55,56,58,61,62,66]. The temperature effects on uranium or actinide systems have been studied by means of the self-consistent ab initio lattice dynamics (SCAILD) method [13,53,60,64,65], and classical molecular dynamics with either the embedded atom method (EAM) or with the modified embedded atom method (MEAM) [28–31,33–36,40–44,47–51,54,57,59,63]. Quantum molecular or ab initio molecular dynamics (AIMD) [18,19,21–26,32,37,39,45,46,52,55,56,58,61,62,66] have also been applied to study thermal effects in uranium, but only in conjunction with pseudopotential electronic-structure methods.

As was mentioned in Refs. [36,53,60,64,65], anharmonic effects and conduction electrons play significant roles determining the heat capacity of uranium metal and its alloys and compounds. Ren et al. [39], using the quasi-harmonic Debye–Grüneisen model, calculated the constant-pressure heat capacity (C_p) of α-U in the temperature range up to 900 K. At low temperatures, up to 300 K, the calculated heat capacity has a reasonable agreement with the experimental data of Flotow and Lohr [67] and Jones et al. [68]. However, as temperature increases, there is a substantial underestimation of the quasi-harmonic heat capacity relative to the experimental data [69] with errors of the order of 50%.

Generally, the heat capacity consists of electronic and lattice vibration contributions. In magnetic systems there is a contribution from magnetism as well. We shall define these contributions below in Section 2 and note here that at high temperatures the electronic contribution is proportional to the electronic density of states and the temperature according to the Sommerfeld assumption [70]. This contribution is particularly important for γ-U as we shall show in this article. According to Ref. [36], γ_e (see definition in Section 2) for α-U have been shown to be microstructurally dependent, with an average value of the experimental results to be about 10.12 mJ/(molK^2). To our knowledge, no measurements have been published for γ-U.

Recent AIMD calculations [66] significantly underestimate the heat capacity for γ-U when compared to experimental data [71], especially in the high-temperature region (1300–1400 K). The early measurements by Marchidan and Ciopec [72] suggested very weak temperature dependence of C_p for γ-U, while Gathers [73] proposed a completely

temperature-independent C_p for the liquid. The results of the measurements by Marchidan and Ciopec [72] and Gathers [73] were questioned by Belashchenko et al. [74], who emphasized the importance of the electronic excitations for the heat capacity. This electronic contribution has a substantial temperature dependence, thus contradicting the conclusion of the experiments [72,73].

In this study, we use DFT electronic structure combined with the SCAILD method [75] to determine the Gibbs free energy and heat capacity for high-temperature uranium in the γ phase. This approach is computationally efficient, very robust (insignificant noise), and it accounts for strong anharmonic phonon–phonon interactions. We employed this scheme with good results recently for actinide monocarbides and mononitrides [53,60,65], and graphite [76]. Approximately a decade ago, we predicted dynamical stability of γ-U with this technique, but calculations of thermodynamic properties were not included in that limited study [13].

Related details of the ab initio and CALPHAD computational methods are outlined in Sections 2 and 3, respectively, followed by a presentation of the results in Section 4. Lastly, a summary and concluding remarks are given in Section 5.

2. Ab Initio Computational Methodology

We calculate the Gibbs free energy, F, and heat capacity, C_v or C_p, for γ-uranium using parameter-free first-principles density-functional theory for the electronic structure. The thermodynamic quantities are here divided into contributions from the lattice dynamics and electronic excitations. No explicit electron–phonon coupling term is included in the formulation of the free energy, simply because there is no straightforward way to compute this contribution. We introduce the most general expression for the Gibbs free energy at zero pressure that we consider for γ-U as a function of volume and temperature (V,T):

$$F(V,T) = F_{lat}(V,T) + F_{el}(V,T) + F_{mag}(V,T) \tag{1}$$

Here, F_{lat} is the free energy from lattice vibrations, F_{el} is the electronic free energy, including entropy, and F_{mag} is the magnetic contribution due to classic entropy of magnetic disorder, S_{mag};

$$F_{mag}(V,T) = -k_B T S_{mag} = -k_B T ln(2\mu + 1) \tag{2}$$

where k_B is the Boltzmann constant and μ is the total magnetic moment (spin and orbital contributions) [77,78]. In an analogous fashion to the free energy, we express and calculate the heat capacity:

$$C_p(T) = C_p^{lat}(T) + C_p^{el}(T) + C_p^{mag}(T) \tag{3}$$

As mentioned in the introduction, under the Sommerfeld assumption [70], the electronic contribution to the specific heat, C_p^{el}, is derived from the electronic density of states, $D(E)$, at the highest occupied energy state (Fermi level, E_F), $D(E_F)$:

$$C_p^{el}(T) = \frac{\pi^2}{3} D(E_F) k_B^2 T = \gamma_e T \tag{4}$$

Note that $D(E)$ depends on temperature in two ways. First, it is broadened by a Fermi–Dirac temperature distribution. Second, it is sensitive to the atomic volume that is increasing with temperature due to thermal volume expansion. We account for both these effects when determining C_p^{el}.

Finally, the magnetic term in Equation (3), C_p^{mag}, is acquired from the following thermodynamic equation at constant pressure [79]:

$$C_p^{mag}(T) = k_B T \left[\frac{dS_{mag}(T)}{dT} \right]_p \tag{5}$$

where the magnetic entropy, S_{mag}, is expressed in Equation (2). Analogous to the electronic contribution, the magnetic term depends on temperature via the electronic structure and thermal expansion.

The electronic and magnetic terms (F_{el}, F_{mag}, C_p^{el}, and C_p^{mag}) are calculated using a very flexible and reliable all-electron full-potential linear muffin-tin orbital (FPLMTO) method [80]. The framework for this method is built on basis functions where the radial part is a linear superposition of atomic-like functions and their derivatives. What makes this implementation different and more flexible than most others is that the basis set can describe energy levels associated with atomic states with separate quantum numbers while having identical magnetic quantum numbers. In other words, for uranium, 6s and 6p states can be represented as well as 7s and 7p states. In some approaches, these states with the same quantum number are defined by a single set of energy parameters in separate energy panels. However, sometimes these panels can intersect, causing numerical problems. Contrarily, in the present FPLMTO approach bases belonging to the same quantum numbers are composed within one fully hybridizing basis set.

Some quantities in FPLMTO are represented in series (bases, charge densities, and potentials) of spherical harmonics inside muffin-tin spheres located on the crystal atomic positions. The radial portion of the muffin-tin-sphere basis function is determined by solving a wave equation that acknowledges all relativistic corrections such as the spin–orbit coupling for d and f states only, i.e., spin–orbit coupling is ignored for p states. The reason for this choice has been discussed and evaluated rather thoroughly for actinide materials [81]. The generalized gradient approximation (GGA) is known to be exceptional for actinides [82] and we apply it here for the electron exchange and correlation functional.

Uranium metal is nonmagnetic at ambient conditions in the ground-state orthorhombic α phase, but it is very close to a magnetic instability that depends sensitively on the volume and crystal structure [83]. Because we are studying uranium at high temperatures, there is a significant thermal expansion and a transition to the bcc γ phase that set the stage for magnetism [83]. Our model therefore includes magnetic interactions and we found that a ferromagnetic alignment of the magnetic moments is favored energetically over the most trivial antiferromagnetic configuration. The trivial antiferromagnetic system is accomplished by repeating the cell once in the *z*-axis direction with spins aligning in opposite directions. For this reason, and the fact that the spin moments disorder at elevated temperatures, we assume ferromagnetic order in our ab initio model for γ-U.

To obtain as accurate total magnetic moments as possible, we apply orbital polarization (OP) for better orbital moments. The DFT + OP approach has been very effective for plutonium metal [84], and even though orbital polarization is almost negligible for α-U [81], it shall not be ignored for γ-U. The orbital-polarization coupling can only happen if there is a charge current, and it is thus not addressed in traditional current-free density-functional theory. Generally, results from the present DFT + OP scheme (see more technical details and references in [84] or [85]) compare excellently with those computed from an approach where orbital polarization is rigorously formulated within an advanced current density-functional theory [86].

The lattice-dynamics contributions to the Gibbs free energy and heat capacity (F_{lat} and C_p^{lat}) are obtained from the SCAILD method that was described in [75]. The method requires calculations of forces on thermally perturbed atoms in a supercell representation of the crystal phase. In this case, we set up a 3^3 (27 atoms) supercell of bcc (γ) uranium and perform 400 SCAILD iterations to ensure very good convergency of the free energy and heat capacity. The supercell size is consistent with our previous SCAILD works [13,53,60,65] and is assumed to be sufficient. Three strategic volumes and six temperatures are simulated with this approach. The SCAILD free-energy volume dependence is obtained by interpolating a cubic polynomial between the three volumes. Atomic forces can be determined from applying the FPLMTO method [13], but it is computationally far easier to utilize a pseudopotential plane-wave-based method, namely, the Vienna ab initio simulation package (VASP) in conjunction with the projector-augmented-wave (PAW) method [87,88].

One important aspect of the calculation is the energy cut-off that defines the expansion of the plane waves in the method. In our previous studies involving SCAILD and force calculations using VASP-PAW [65], we found that a plane-wave energy cut-off of about 400 eV is reasonably accurate. However, in the present case of γ-uranium, we checked the influence of a greater energy cut-off (500 eV) on one temperature and volume (1000 K and 20.86 Å^3). The lattice contribution to the free energy changed with these more accurate calculations, but only by a small amount of about 0.24 meV.

In analogy with the all-electron FPLMTO treatment, we assumed ferromagnetic order in the VASP calculations of the forces for SCAILD. Furthermore, again consistent with the all-electron approach, the VASP calculations relied on the generalized gradient approximation for the electron interactions. For the spin–orbit interaction, we implemented [81] the same correction as with the FPLMTO and included the orbital-polarization scheme. One difference with VASP relative to FPLMTO is that we apply a fixed 5f-electron Racah parameter (0.056 eV) in VASP. The parameter value is determined using the Racah parameters that are self-consistently calculated within the all-electron approach. Because of the coupling between DFT, OP, and SCAILD, we refer to the complete theoretical approach as DFT + OP + SCAILD.

3. CALPHAD Methodology

The CALPHAD method (CALculation of PHAse Diagrams) is aimed at calculating phase diagrams from primarily experimental data but also from results obtained from first-principles theory. One unique feature is that it can be used to establish a thermodynamic database for metastable phases. For example, CALPHAD can be applied to compute thermodynamic properties of γ-uranium at temperatures lower than its field of stability (1048.99 K). CALPHAD uses mean field theory and models to represent thermodynamic functions such as the Gibbs free energy.

Here, we apply CALPHAD to compute the Gibbs energy and heat capacity at constant pressure of γ-uranium. The CALPHAD results are very important because—as Gibbs free energies cannot be measured directly experimentally—they can be directly compared to the ab initio results (i.e., Gibbs free energy) that we present in this article. The method uses mathematical models to describe Gibbs free energy functions for a given phase as a function of temperature, composition, and pressure. In this case, we do not consider composition as we focus on unalloyed uranium. The method fits to experimental thermodynamic data but not the Gibbs free energy itself [89,90]. The functions are stored in a thermodynamic database and used for equilibrium (ambient pressure) calculations of a given system. In this study, we use the Thermo-Calc software version 2022b [91] and adopt the thermodynamic description in the PURE5 database [92] which is based on Ref. [93] for unary (elemental) data.

4. Results

First, we compile some results for γ-U at zero or room temperature in Table 1. Of course, γ-U does not exist at low temperatures, but it is still useful to compare different modeling approaches. Experimentally, an estimate of the room-temperature atomic volume from extrapolating molybdenum-stabilized γ-U to zero Mo content was suggested (20.89 Å^3) [94]. The experimental bulk modulus for γ-U was obtained from extrapolating diamond anvil cell compression data to zero pressure [14].

The MEAM potential [30] is developed by fitting model parameters to various physical properties of uranium metal obtained from experiments and theory. The MEAM results are relatively close to experimental data for γ-U, suggesting a reasonable parameterization of the MEAM, although the γ-U volume is overestimated by almost 3%. All pseudopotential results, on the other hand, underestimate the volume by about 3–9%, while overestimating the bulk modulus by about 16–56%. For DFT modeling, this level of error is noteworthy.

Table 1. Room-temperature atomic volume (Å^3) and bulk modulus (GPa) for γ-U from present theory (DFT + OP + SCAILD), other modeling, and experiments.

Method	Atomic Volume (Å^3)	Bulk Modulus (GPa)
MEAM [30]	21.49	115
Pseudopotential [95]	19.06	170
Pseudopotential [19]	20.18	176
Pseudopotential [96]	20.32	133
Pseudopotential [32]	20.12	132
All-electron [15]	20.76	120
All-electron DFT + OP + SCAILD	21.00	114
Experiment [14,94]	20.89	113

The all-electron results show the best agreement with experiment, with more acceptable errors of <1% in volume and ~1–6% in the bulk modulus. There is a small difference between the 2002 all-electron data [15] and the present DFT + OP + SCAILD, and the reason is numerical. The earlier calculation [15] applied a 20 mRy Gaussian broadening to the energy eigenvalues, while in the present study it is replaced by a 300 K Fermi–Dirac distribution. Normally, one would not expect any meaningful volume dependence on the electronic-structure broadening, and it is also not large here. However, γ-U has very narrow 5f bands at the Fermi level, the reason for its dynamical instability, which causes this sensitivity. For α-U, the corresponding density of states is much lower, resulting in less consequence of the broadening scheme; see further discussions in this section below.

In Figure 1, we show our calculated volume expansion for γ-U together with results from AIMD [46,66], MEAM [30], and experiments [97,98].
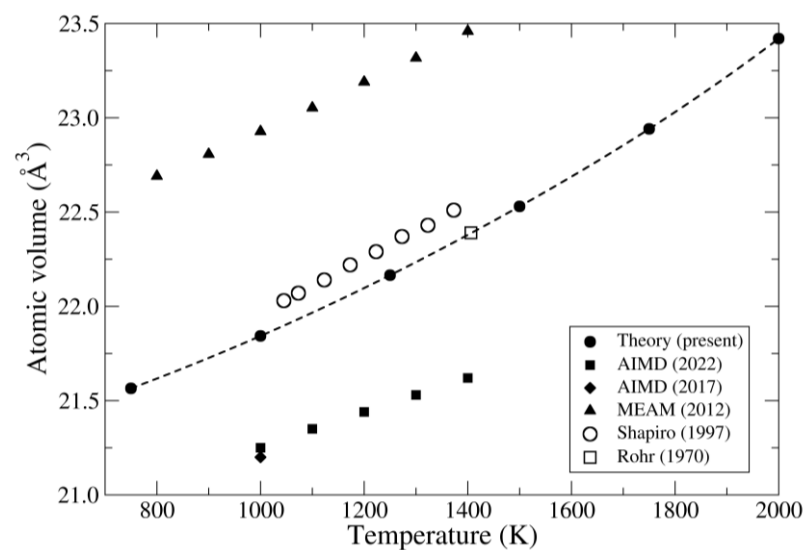
Figure 1. Atomic volumes (Å^3) for γ-U as functions of temperature. Solid symbols represent our DFT + OP + SCAILD model, AIMD [46,66], and MEAM results [30]. Open symbols indicate experimental data [97,98]. The dashed line is provided only as a guide. γ-U melts at 1408 K and theoretical data points above that temperature are shown for a hypothetical γ-U solid phase.

Our theory (solid circles and dashed line) in Figure 1 agrees very well with the experimental data [97,98]; only a very small shift is evident relative to one experimental set [97]. The small errors (<1%) are consistent with the findings for the low-temperature volume in Table 1. The MEAM results overestimate the volumes by about 4% and are also consistent with the low-temperature data in Table 1. The AIMD modeling, on the other hand, underestimates the volumes by about 3.5%, as is expected from the results in Table 1. The slopes of the curves (change of volume with temperature) suggest that

DFT + OP + SCAILD and the MEAM results are in better agreement with the experimental trend than AIMD, which indicates a too-small thermal expansion. In principle, the AIMD treatment is more complete than SCAILD for lattice dynamics, but the results of Figure 1 suggest that SCAILD is more accurate in practice for γ-U.

Next, we will discuss our results for the Gibbs free energy. Our calculated γ-U equilibrium volumes in Figure 1 are determined as the volumes that define the minimum of the Gibbs free energy, Equation (1), as a function of temperature. In our approach, we include three contributions to the free energy. The terms F_{el} and F_{mag} are calculated for a one-atom bcc cell, utilizing the all-electron FPLMTO method. The lattice contribution, F_{lat}, is obtained from SCAILD where the atomic forces are calculated with the VASP-PAW method. Both electronic-structure methods represent the DFT + OP approach.

In Table 2, we show our calculated magnetic moments and the separate contributions to the Gibbs free energy as functions of temperature.

Table 2. Spin (μ_{spin}) and orbital ($\mu_{orbital}$) magnetic moments (μ_B) and Gibbs free energy contributions (eV) as functions of temperature obtained from our DFT + OP + SCAILD model. F_{el} energies are shifted to zero at zero temperature.

Temperature	μ_{spin}	$\mu_{orbital}$	F_{mag}	F_{el}	F_{lat}
750	0.1150	−0.0870	−0.0035	−0.0053	−0.4342
1000	0.1383	−0.1088	−0.0049	−0.0239	−0.6572
1250	0.1580	−0.1290	−0.0061	−0.0470	−0.9005
1500	0.1740	−0.1480	−0.0066	−0.0738	−1.1571
1750	0.1860	−0.1650	−0.0062	−0.1041	−1.4362
2000	0.1950	−0.1810	−0.0048	−0.1372	−1.7264

We see in Table 2 that the magnetic contribution to the free energy is of the same order as the electronic contribution at 750 K, but at higher temperatures it becomes rather small even though the magnetic moments are far from negligible. For actinides with less than half-full 5f-band occupations, such as uranium, contributions to the total magnetic moment, i.e., spin and orbital components, have antiparallel directions so that the net moment is largely suppressed due to the compensation. We note that the magnetic moments increase in magnitude with temperature, but the total moment, due to a relatively increasing fraction of the orbital component, decreases weakly above 1000 K. Overall, however, the thermal dependence of the net magnetism is rather small.

It is not possible to measure the free energy directly for any material, and therefore an explicit comparison between our model and experiment is not conceivable. Nonetheless, the CALPHAD approach allows for a free-energy representation of available experimental thermodynamic data, and here, we compare our ab initio model with CALPHAD in Figure 2. We are not surprised to find that DFT + OP + SCAILD is very close to the CALPHAD results for γ-U. In our recent focus on actinide systems, we found very good agreement between the two approaches for Gibbs free energy [65]. Unfortunately, we were not able to find any other published modeling data on Gibbs free energy for γ-U that we could compare our predictions with.

Next, we focus on the heat capacity that consists of terms (Equation (3)) analogous to the free energy (Equation (1)). In practice, we ignore the C_p^{mag} term, because, numerically, the total magnetic moment is nearly constant with temperature. The lattice-vibration term, C_p^{lat}, is dominating, but the electronic contribution, C_p^{el}, cannot be neglected at elevated temperatures. The reason is that the electronic density of states is quite high at the Fermi level and C_p^{el} is proportional to this quantity and temperature; see Equation (4).
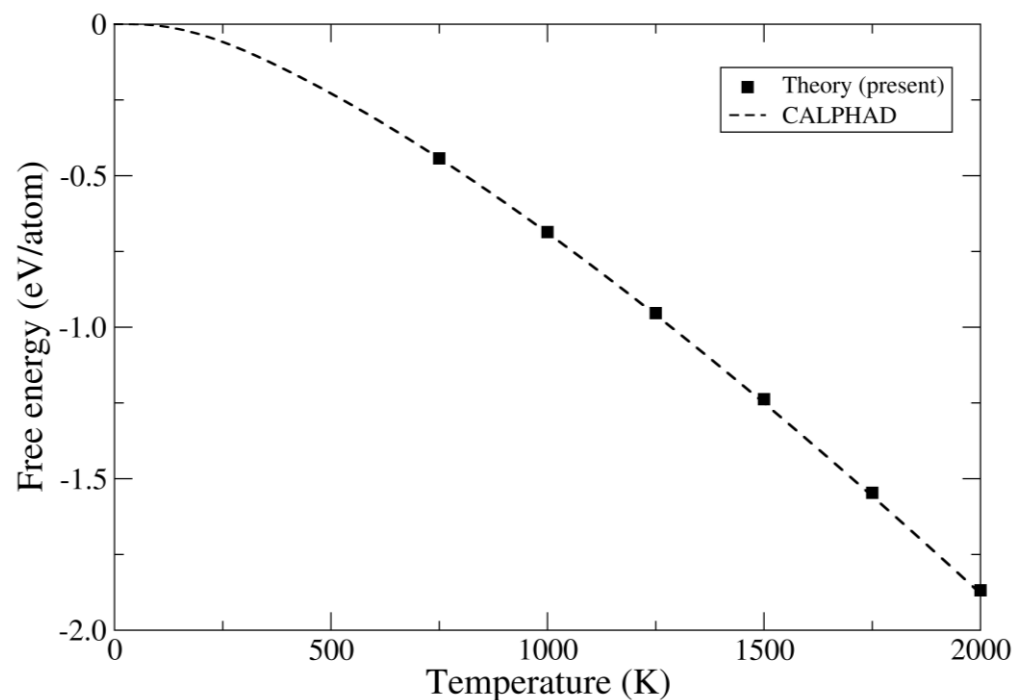
Figure 2. Gibbs free energy for γ-U from our DFT + OP + SCAILD and CALPHAD. Data below 300 K for CALPHAD are interpolated to zero temperature. Theoretical data points above the melting temperature (1408 K) are shown for a hypothetical γ-U solid phase.

In Figure 3, we show electronic density of states for α- and γ-uranium, at atomic volumes corresponding to 300 K (α) and 1250 K (γ), respectively. The density of states at the dashed vertical line (Fermi level) for γ-U is almost double that of α-U. This explains why the α phase is the ground state and not γ, as we discussed in terms of a Peierls-type crystal distortion in the introduction. γ-U is, however, dynamically stable at high temperatures. For the γ phase, the high density of states contributes to a large electronic contribution to the heat capacity that is linear with temperature; see Equation (4). The calculated γ_e is about 10.6 mJ/(molK^2), which is close to what has been measured for α-U [36]. The electronic heat capacity is thus predicted to be quite significant for γ-U. That is important, because the experimental data are rather scattered, as we shall see below, and the high-temperature behavior is not conclusively determined.

In Figure 4, we present heat capacities from our DFT + OP + SCAILD approach, AIMD [66], together with CALPHAD and data from the experimental reports [71,72]. Konings and Beneš [71] used a polynomial equation for the heat capacity to fit experimental enthalpy-increment data from multiple authors [72,99–101]. We conducted our own fit and constrained C_p at 298.15 K while also adjusting for the β–γ transition. The resulting C_p has decidedly less temperature dependence. Our fit is a more consistent representation of the heat capacity that clearly falls within the range of derived experimental value [72,99–101]. Adapting an arbitrary polynomial function that can take any form of $C_p = a + bT + cT^2 + dT^{-2}$ to enthalpy-increment data may explain the scatter observed in Figure 4, whereas the measured data, (enthalpy-increment, not heat capacity) of [72,99–101] are all consistent with each other, as described by Konings and Beneš [71]. Interestingly, some of the C_p data obtained this way show a negative trend with temperature, particularly [102]. Because C_v is bound by the law of Dulong and Petit (classical asymptotic limit), and C_p for most solids has a positive temperature-dependent correction to C_v [103], the negative thermal behavior of these data seems odd.
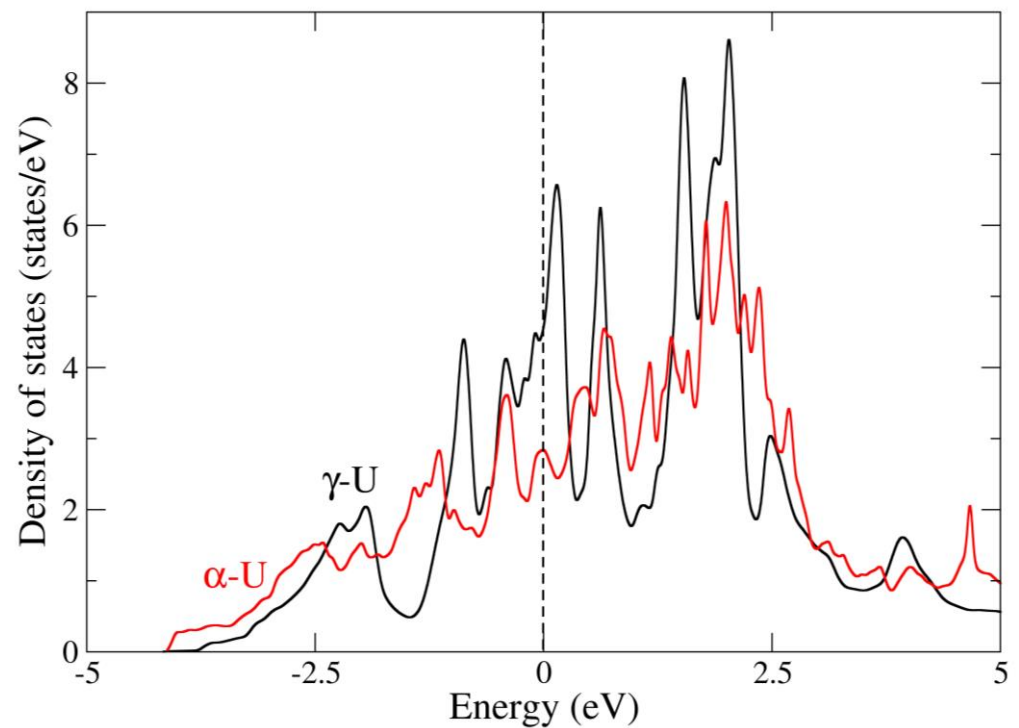
Figure 3. Electronic density of states (states/eV) for α-U (solid red) and γ-U (solid black) at volumes corresponding to 300 K and 1250 K, respectively. The energies are shifted so that the Fermi level is at zero energy, indicated with a dashed vertical line. For better readability, we apply a 2 mRy Gaussian broadening to the density of states.
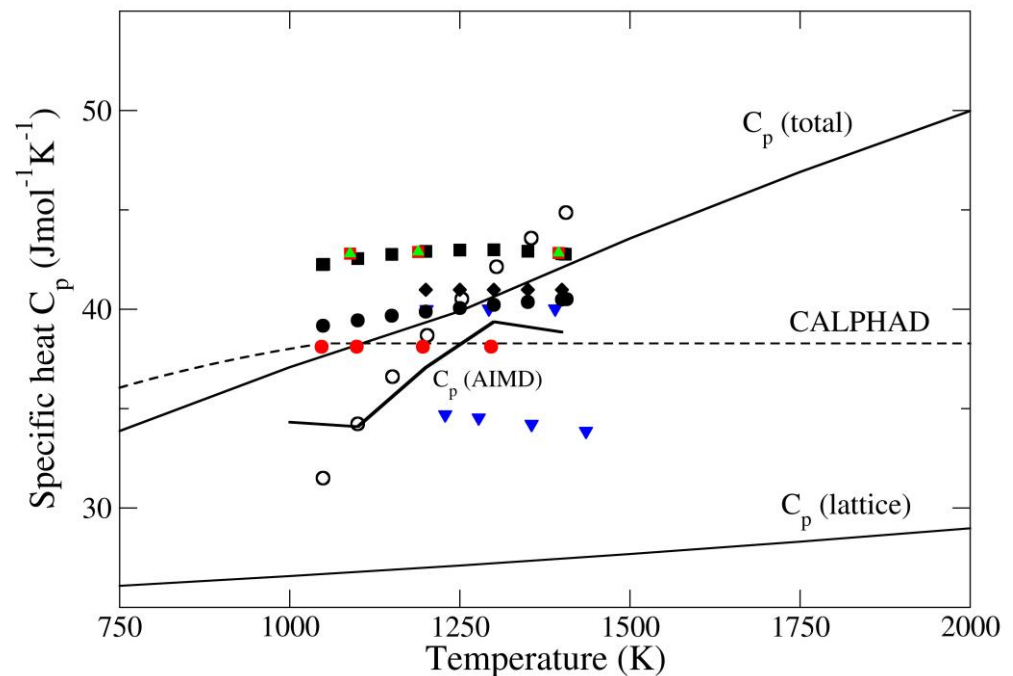
Figure 4. Specific heat from DFT + OP + SCAILD and AIMD [66] (solid lines), CALPHAD (dashed line), and data derived from experimental enthalpy results [71] (open circles), our own analysis of the data [71] (solid circles) (see main text), [99] (green triangles), [100] (red circles), [101] (solid diamonds), [102] (blue triangles), and [104] (red squares). C_p (lattice) is the DFT + OP + SCAILD result without the electronic contribution, and C_p (total) includes it. Theoretical data points above the melting temperature are shown for a hypothetical γ-U solid phase.

Our "C$_p$ (total)" results in Figure 4 are in reasonable agreement with our adjusted values from [71] and fall within the bounds of the various experimentally derived heat capacity data [72,99–101]. The CALPHAD results indicate a slope before about 1050 K, after which a constant value is assumed. This behavior is compatible with the data from Moore [99], Ginnings [100], and the review compiled by Rand and Kubaschewski [102] on which the data of Dinsdale [93] is based. The abrupt change after 1050 K in the CALPHAD data is likely related to the β–γ transition in uranium.

We notice that the AIMD C_p shows an interesting *S* shape that does not correlate with experiment or our ab initio model or CALPHAD, but the general trend is an increase with temperature. In addition, the AIMD predicts too-small C_p at the highest temperatures close to 1400 K, as Aly et al. point out in their report [66].

Our DFT + OP + SCAILD predictions in the 1050–1408 K stability domain of γ-U are comfortably within the scatter of the heat-capacity data derived from the measured enthalpy increments. Although most of these data appear to suggest only weak temperature dependence, our theory clearly indicates a slope of the C_p curve.

5. Summary and Conclusions

We computed thermodynamic properties for γ-U using the DFT + OP + SCAILD technique. Aside from a more limited study on the dynamical stability [13], this approach has not previously been employed for γ-U. All quantities were obtained from a very accurate all-electron method, except for the atomic forces needed for the lattice dynamics that were, for expedience, calculated with the more approximate pseudopotential method. Both techniques include relativistic and magnetic interactions in terms of spin–orbit coupling and orbital polarization. The thermal expansion and large volume (relative to α-U) of γ-U induces significant polarization of the electronic structure, and the model predicts formation of spin and orbital moments. The relativistic and magnetic interactions lower the electronic energy, and the magnetic moments provide an entropy contribution to Gibbs free energy. The temperature dependence of the Gibbs free energy contribution from these interactions is calculated to be relatively small, 0.021 eV, between 750 and 1250 K. Nevertheless, this difference is noticeable on the scale in Figure 2, and neglecting magnetic interactions worsens the agreement with CALPHAD. The good agreement between our ab initio modeling and CALPHAD computations gives credence to both approaches.

The lack of relativistic and magnetic correlations In the AIMD electronic structure [66], for example, is not the main cause for the poorly estimated γ-U volumes in Figure 1, but rather the limitation of the pseudopotential approximation. This becomes clear in Table 1, where all pseudopotential calculations strongly underestimate the γ-U volume at low temperatures, contrarily to the all-electron results.

One of the driving motivations for our study is to shed light on uranium's thermal behavior of the heat capacity at high temperatures. The experimental data are rather scattered with weak temperature dependence, but our DFT + OP + SCAILD calculations indicate an increase of the specific heat with temperature. In our view, it is not likely that the high-temperature heat capacity completely lacks thermal dependence for γ-U because of the non-negligible electronic contribution. The thermal behavior matters because a stronger thermal dependence affects thermal transport predictions of fuel fabrication processes such as casting and forming. The modified properties will hopefully lead to more accurate predictions which can improve efficiency and lower cost of production.

Author Contributions: Conceptualization, P.S. and A.L.; methodology, P.S., A.L., A.P. and E.E.M.; software, P.S., A.L., A.P. and E.E.M.; investigation, P.S., A.L., A.P. and E.E.M.; writing—original draft preparation, A.L. and P.S.; writing—review and editing, P.S., A.L., A.P., E.E.M., J.R. and J.T.M. All authors have read and agreed to the published version of the manuscript.

Conflicts of Interest: The authors declare no conflict of interest.

References

1. Hofman, G.; Walters, L.; Bauer, T. Metallic fast reactor fuels. *Prog. Nucl. Energy* **1997**, *31*, 83–110. [CrossRef]
2. Meyer, M.K.; Hofman, G.L.; Hayes, S.L.; Clark, C.R.; Wiencek, T.C.; Snelgrove, J.L.; Strain, R.V.; Kim, K.-H. Low-temperature irradiation behavior of uranium–molybdenum alloy dispersion fuel. *J. Nucl. Mater.* **2002**, *304*, 221–236. [CrossRef]
3. Kim, Y.S.; Hofman, G.; Yacout, A. Migration of minor actinides and lanthanides in fast reactor metallic fuel. *J. Nucl. Mater.* **2009**, *392*, 164–170. [CrossRef]
4. Carmack, W.J.; Porter, D.L.; Chang, I.; Hayes, S.L.; Meyer, M.K.; Burkes, D.E.; Lee, C.B.; Mizuno, T.; Delage, F.; Somers, J.; et al. Metallic fuels for advanced reactors. *J. Nucl. Mater.* **2009**, *392*, 139–150. [CrossRef]
5. Todreas, N.E. Thermal-hydraulics challenges in fast reactor design. *Nucl. Tech.* **2009**, *167*, 127–144. [CrossRef]
6. Janney, D.E. *Metallic Fuels Handbook, Part 1: Alloys Based on U-Zr, Pu-Zr, U-Pu, or U-Pu-Zr, Including Those with Minor Actinides (Np, Am, Cm) Rare-Earth Elements (La, Ce, Pr, Nd, Gd), and Y*; Idaho National Laboratory: Idaho Falls, ID, USA, 2017.
7. Capriotti, L.; Bremier, S.; Inagaki, K.; Poml, P.; Papaioannou, D.; Ohta, H.; Ogata, T.; Rondinella, V.V. Characterization of metallic fuel for minor actinides trans mutation in fast reactor. *Prog. Nucl. Energy* **2017**, *94*, 194–201. [CrossRef]
8. Imhoff, S.D. *Uranium Density, Thermal Conductivity, Specific Heat, and Thermal Diffusivity*; LA-UR-21-21810; OSTI.GOV: Idaho National Lab: Idaho Falls, ID, USA, 24 February 2021.
9. Söderlind, P. Theory of the crystal structures of cerium and the light actinides. *Adv. Phys.* **1998**, *47*, 959–998. [CrossRef]
10. Söderlind, P.; Johansson, B.; Yongming, L.; Nordström, L. Calculated thermal expansion of the actinide elements. *Int. J. Thermophys.* **1991**, *12*, 611–615. [CrossRef]
11. Söderlind, P.; Eriksson, O.; Wills, J.M.; Boring, A.M. Elastic constants of cubic *f*-electron elements: Theory. *Phys. Rev. B* **1993**, *48*, 9306–9312. [CrossRef]
12. Söderlind, P.; Eriksson, O.; Wills, J.; Boring, A. A unified picture of the crystal structures of metals. *Nature* **1995**, *374*, 524–525. [CrossRef]
13. Söderlind, P.; Grabowski, B.; Yang, L.; Landa, A.; Björkman, T.; Souvatzis, P.; Eriksson, O. High-temperature phonon stabilization of γ-uranium from relativistic first-principles theory. *Phys. Rev. B* **2012**, *85*, 60301. [CrossRef]
14. Yoo, C.-S.; Cynn, H.; Söderlind, P. Phase diagram of uranium at high pressures and temperatures. *Phys. Rev. B* **1998**, *57*, 10359. [CrossRef]
15. Söderlind, P. First-principles elastic and structural properties of uranium metal. *Phys. Rev. B* **2002**, *66*, 85113. [CrossRef]
16. Wills, J.M.; Eriksson, O. Crystal-structure stabilities and electronic structure for the light actinides Th, Pa, and U. *Phys. Rev. B* **1992**, *45*, 13879. [CrossRef]
17. Richard, N.; Bernard, S.; Jollet, F.; Torrent, M. Plane-wave pseudopotential study of the light actinides. *Phys. Rev. B* **2002**, *66*, 235112. [CrossRef]
18. Hood, R.; Yang, L.H.; Moriarty, J. Quantum molecular dynamics simulations of uranium at high pressure and temperature. *Phys. Rev. B* **2008**, *78*, 24116. [CrossRef]
19. Taylor, C.D. Evaluation of first-principles techniques for obtaining materials parameters of alpha uranium and the (001) alpha uranium surface. *Phys. Rev. B* **2008**, *77*, 94119. [CrossRef]
20. Xiang, S.; Huang, H.; Hsiung, L.M. Quantum mechanical calculations of uranium phases and niobium defects in γ-uranium. *J. Nucl. Mater.* **2008**, *375*, 113–119. [CrossRef]
21. Bouchet, J. Lattice dynamics of α uranium. *Phys. Rev. B* **2008**, *77*, 24113. [CrossRef]
22. Beeler, B.; Good, B.; Rashkeev, S.; Deo, C.; Baskes, M.; Okuniewski, M. First principles calculations for defects in U. *J. Phys. Condens. Matter.* **2010**, *22*, 505703. [CrossRef]
23. Raymond, S.; Bouchet, J.; Lander, G.H.; Le Tacon, M.; Garbarino, G.; Hoesch, M.; Rueff, J.-P.; Krisch, M.; Lashley, J.C.; Schulze, R.K.; et al. Understanding the complex phase diagram of uranium: The role of electron-phonon coupling. *Phys. Rev. Lett.* **2011**, *107*, 136401. [CrossRef]
24. Bouchet, J.; Albers, R. Elastic properties of the light actinides at high pressure. *J. Phys. Condens. Matter.* **2011**, *23*, 215402. [CrossRef] [PubMed]
25. Huang, G.-Y.; Wirth, B.D. First-principles study of diffusion of interstitial and vacancy in α U-Zr. *J. Phys. Condens. Matter* **2011**, *23*, 205402. [CrossRef] [PubMed]
26. Huang, G.-Y.; Wirth, B.D. First-principles study of bubble nucleation and growth behaviors in α U-Zr. *J. Phys. Condens. Matter* **2012**, *24*, 415404. [CrossRef]
27. Akella, J.; Weir, S.; Wills, J.M.; Söderlind, P. Structural stability in uranium. *J. Phys. Condens. Matter* **1997**, *9*, L549–L555. [CrossRef]
28. Smirnova, D.E.; Starikov, S.V.; Stegailov, V.V. Interatomic potential for uranium in a wide range of pressures and temperatures. *J. Phys. Condens. Matter.* **2012**, *24*, 15702. [CrossRef] [PubMed]

29. Smirnova, D.E.; Starikov, S.V.; Stegailov, V.V. New interatomic potential for computation of mechanical and thermodynamic properties of uranium. *Phys. Met. Metallogr.* **2012**, *113*, 107–116. [CrossRef]

30. Beeler, B.; Deo, C.; Baskes, M.; Okuniewski, M. Atomistic properties of γ uranium. *J. Phys. Condens. Matter* **2012**, *24*, 75401. [CrossRef]

31. Pascuet, M.I.; Bonny, G.; Fernández, J.R. Many-body interatomic U and Al–U potentials. *J. Nucl. Mater.* **2012**, *424*, 158–163. [CrossRef]

32. Beeler, B.; Deo, C.; Baskes, M.; Okuniewski, M. First principles calculations of the structure and elastic constants of α, β and γ uranium. *J. Nucl. Mater.* **2013**, *433*, 143–151. [CrossRef]

33. Smirnova, D.E.; Kuksin, A.Y.; Starikov, S.V.; Stegailov, V.V.; Insepov, Z.; Rest, J.; Yacout, A.M. A ternary EAM interatomic potential for U–Mo alloys with xenon. *Modell. Simul. Mater. Sci. Eng.* **2013**, *21*, 35011. [CrossRef]

34. Smirnova, D.E.; Kuksin, A.Y.; Starikov, S.V. Investigation of point defects diffusion in bcc uranium and U–Mo alloys. *J. Nucl. Mater.* **2015**, *458*, 304–311. [CrossRef]

35. Smirnova, D.E.; Kuksin, A.Y.; Starikov, S.V.; Stegailov, V.V. Atomistic modeling of the self-diffusion in γ-U and γ-U–Mo. *Phys. Met. Metallogr.* **2015**, *116*, 445–455. [CrossRef]

36. Moore, A.P.; Beeler, B.; Deo, C.; Baskes, M.I.; Okuniewski, M.A. Atomistic modeling of high temperature uranium-zirconium alloy structure and thermodynamics. *J. Nucl. Mater.* **2015**, *467*, 802–819. [CrossRef]

37. Bouchet, J.; Bottin, F. Thermal evolution of vibrational properties of α-U. *Phys. Rev. B* **2015**, *92*, 174108. [CrossRef]

38. Tseplyaev, V.I.; Starikov, S.V. The atomistic simulation of pressure-induced phase transition in uranium mononitride. *J. Phys. Conf. Ser.* **2015**, *653*, 012092. [CrossRef]

39. Ren, Z.; Wu, J.; Ma, R.; Hu, G.; Luo, C. Thermodynamic properties of α-uranium. *J. Nucl. Mater.* **2016**, *480*, 80–87. [CrossRef]

40. Kuksin, A.Y.; Starikov, S.V.; Smirnova, D.E.; Tseplyaev, V.I. The diffusion of point defects in uranium mononitride: Combination of DFT and atomistic simulation with novel potential. *J. Alloys Comp.* **2016**, *658*, 385–394. [CrossRef]

41. Kolotova, L.N.; Kuksin, A.Y.; Smirnov, D.E.; Starikov, S.V.; Tseplyaev, V.I. Features of structure and phase transitions in pure uranium and U–Mo alloys: Atomistic simulation. *J. Phys. Conf. Ser.* **2016**, *774*, 12036. [CrossRef]

42. Kolotova, L.N.; Starikov, S.V. Anisotropy of the U–Mo alloy: Molecular-dynamics study. *Phys. Met. Metallogr.* **2016**, *117*, 487–493. [CrossRef]

43. Tseplyaev, V.I.; Starikov, S.V. The atomistic simulation of pressure-induced phase transition in uranium mononitride. *J. Nucl. Mater.* **2016**, *480*, 7–14. [CrossRef]

44. Starikov, S.V.; Kolotova, L.N. Features of cubic and tetragonal structures of U–Mo alloys: Atomistic simulation. *Script. Mater.* **2016**, *113*, 27–30. [CrossRef]

45. Huang, S.-Q.; Ju, X.-H. First-principles study of properties of alpha uranium crystal and seven alpha-uranium surfaces. *J. Chem.* **2017**, *2017*, 8618340. [CrossRef]

46. Bouchet, J.; Bottin, F. High-temperature and high-pressure phase transitions in uranium. *Phys. Rev. B* **2017**, *95*, 54113. [CrossRef]

47. Kolotova, L.N.; Starikov, S.V. Atomistic simulation of defect formation and structure transitions in U-Mo alloys in swift heavy ion irradiation. *J. Nucl. Mater.* **2017**, *495*, 111–117. [CrossRef]

48. Starikov, S.; Kuksin, A.; Smirnova, D.; Dolgodvorov, A.; Ozrin, V. Multiscale modeling of uranium mononitride: Point defects diffusion, self-diffusion, phase composition. *Defect Diffus. Forum* **2017**, *375*, 101–113. [CrossRef]

49. Starikov, S.V.; Kolotova, L.N.; Kuksin, A.Y.; Smirnova, D.E.; Tseplyaev, V.I. Atomistic simulation of cubic and tetragonal phases of U-Mo alloy: Structure and thermodynamic properties. *J. Nucl. Mater.* **2018**, *499*, 451–463. [CrossRef]

50. Starikov, S.; Korneva, M. Description of phase transitions through accumulation of point defects: UN, UO$_2$ and UC. *J. Nucl. Mater.* **2018**, *510*, 373–381. [CrossRef]

51. Lunev, A.V.; Starikov, S.V.; Aliev, T.N.; Tseplyaev, V.I. Understanding thermally-activated glide of 1/2 110 {110} screw dislocations in UO$_2$—A molecular dynamics analysis. *Intern. J. Plast.* **2018**, *110*, 294–305. [CrossRef]

52. Torres, E.; Kaloni, T.P. Projector augmented-wave pseudopotentials for uranium-based compounds. *Comp. Mater. Sci.* **2020**, *171*, 109237. [CrossRef]

53. Söderlind, P.; Landa, A.; Perron, A.; Sadigh, B.; Heo, T.W. Ground-state and thermodynamical properties of uranium mononitride from anharmonic first-principles theory. *Appl. Sci.* **2019**, *9*, 3914. [CrossRef]

54. Kolotova, L.N.; Starikov, S.V.; Ozrin, V.D. Atomistic simulation of the fission-fragment-induced formation of defects in a uranium–molybdenum alloy. *J. Exp. Theor. Phys.* **2019**, *129*, 59–65. [CrossRef]

55. Castellano, A.; Bottin, F.; Dorado, B.; Bouchet, J. Thermodynamic stabilization of γ-U-Mo alloys: Effect of Mo content and temperature. *Phys. Rev. B* **2020**, *101*, 184111. [CrossRef]

56. Ladygin, V.V.; Korotaev, P.Y.; Yanilkin, A.V.; Shapeev, A.V. Lattice dynamics simulation using machine learning interatomic potentials. *Comput. Mater. Sci.* **2020**, *172*, 109333. [CrossRef]

57. Beeler, B.; Casagranda, A.; Aagesen, L.; Zhang, Y.; Novascone, S. Atomistic calculations of the surface energy as a function of composition and temperature in γ U-Zr to inform fuel performance modeling. *J. Nucl. Mater.* **2020**, *540*, 152271. [CrossRef]

58. Beeler, B.; Andersson, D.; Jiang, C.; Zhang, Y. Ab initio molecular dynamics investigation of point defects in γ-U. *J. Nucl. Mater.* **2020**, *545*, 152714. [CrossRef]

59. Kolotova, L.; Gordeev, I. Structure and phase transition features of monoclinic and tetragonal phases in U–Mo alloys. *Crystals* **2020**, *10*, 515. [CrossRef]

60. Söderlind, P.; Landa, A.; Perron, A.; Moore, E.E.; Wu, C. Thermodynamics of plutonium monocarbide from anharmonic and relativistic theory. *Appl. Sci.* **2020**, *10*, 6524. [CrossRef]
61. Beeler, B.; Mahbuba, K.; Wang, Y.; Jokisaari, A. Determination of thermal expansion, defect formation energy, and defect-induced strain of α-U via ab initio molecular dynamics. *Front. Mater.* **2021**, *8*, 661387. [CrossRef]
62. Migdal, K.; Yanilkin, A. Cold and hot uranium in DFT calculations: Investigation by the GTH pseudopotential, PAW, and APW + lo methods. *Comput. Mater. Sci.* **2021**, *199*, 110665. [CrossRef]
63. Ouyang, W.; Lai, W.; Li, J.; Liu, J.; Liu, B. Atomic simulations of U-Mo under irradiation: A new angular dependent potential. *Metals* **2021**, *11*, 1018. [CrossRef]
64. Söderlind, P.; Yang, L.H.; Landa, A.; Wu, A. Mechanical and thermal properties for uranium and U–6Nb alloy from first-principles theory. *Appl. Sci.* **2021**, *11*, 5643. [CrossRef]
65. Söderlind, P.; Moore, E.E.; Wu, C.J. Thermodynamics modeling for actinide monocarbides and mononitrides from first principles. *Appl. Sci.* **2022**, *12*, 728. [CrossRef]
66. Aly, A.; Beeler, B.; Avramova, M. Ab initio molecular dynamics investigation of γ-(U,Zr) structural and thermal properties as a function of temperature and composition. *J. Nucl. Mater.* **2022**, *561*, 153523. [CrossRef]
67. Flotow, H.E.; Lohr, H.R. The heat capacity and thermodynamic functions of uranium from 5 to 350 K. *J. Phys. Chem.* **1960**, *64*, 904–906. [CrossRef]
68. Jones, W.; Gordon, J.; Long, E. The heat capacities of uranium, uranium trioxide, and uranium dioxide from 15 K to 300 K. *J. Chem. Phys.* **1952**, *20*, 695–699. [CrossRef]
69. Nakamura, J.-I.; Takashi, Y.; Izumi, S.-I.; Kanno, M. Heat capacity of metallic uranium and thorium from 80 to 1000 K. *J. Nucl. Mater.* **1980**, *88*, 64–72. [CrossRef]
70. Grimvall, G. *Thermophysical Properties of Materials*; Elsevier BV: Amsterdam, The Netherlands, 1999; pp. 157–172.
71. Konings, R.J.M.; Beneš, O. The thermodynamic properties of the f-elements and their compounds. I. The lanthanide and actinide metals. *J. Phys. Chem. Ref. Data* **2010**, *39*, 43102. [CrossRef]
72. Marchidan, D.I.; Ciopec, M. Enthalpy of uranium to 1500 K by drop calorimetry. *J. Chem. Therm.* **1976**, *8*, 691–701. [CrossRef]
73. Gathers, G. Dynamic methods for investigating thermophysical properties of matter at very high temperatures and pressures. *Rep. Prog. Phys.* **1986**, *86*, 341–396. [CrossRef]
74. Belashchenko, D.K.; Smirnova, D.E.; Ostrovsky, O.I. Molecular-dynamic simulation of the thermophysical properties of liquid uranium. *High Temp.* **2010**, *48*, 363–375. [CrossRef]
75. Souvatzis, P.; Eriksson, O.; Katsnelson, M.I.; Rudin, S.P. Entropy driven stabilization of energetically unstable crystal structures explained from first principles theory. *Phys. Rev. Lett.* **2008**, *100*, 95901. [CrossRef] [PubMed]
76. Söderlind, P.; Landa, A.; Hood, R.Q.; Moore, E.E.; Perron, A.; McKeown, J.T. High-temperature thermodynamics modeling of graphite. *Appl. Sci.* **2022**, *12*, 7556. [CrossRef]
77. Grimvall, G. Spin disorder in paramagnetic fcc iron. *Phys. Rev. B* **1989**, *39*, 12300–12301. [CrossRef] [PubMed]
78. Wang, Y. Classical mean-field approach for thermodynamics: Ab initio thermophysical properties of cerium. *Phys. Rev. B* **2000**, *61*, R11863–R11866. [CrossRef]
79. Grimvall, G.; Häglund, J.; Fernández Guillermet, A. Spin fluctuations in paramagnetic chromium determined from entropy considerations. *Phys. Rev. B* **1993**, *47*, 15338–15341. [CrossRef]
80. Wills, J.M.; Eriksson, O.; Andersson, P.; Delin, A.; Grechnyev, O.; Alouani, M. *Full-Potential Electronic Structure Method*; Springer Series in Solid-State Science; Springer: Berlin/Heidelberg, Germany, 2010; Volume 167.
81. Sadigh, B.; Kutepov, A.; Landa, A.; Söderlind, P. Assessing relativistic effects and electron correlation in the actinide metals Th-Pu. *Appl. Sci.* **2019**, *9*, 5020. [CrossRef]
82. Söderlind, P. First-principles phase stability, bonding, and electronic structure of actinide metals. *J. Electron. Spectr. Rel. Phenom.* **2014**, *194*, 2–7. [CrossRef]
83. Söderlind, P.; Moore, K.T. When magnetism can stabilize the crystal structure of metals. *Scripta Mat.* **2008**, *59*, 1259–1262. [CrossRef]
84. Söderlind, P.; Landa, A.; Sadigh, B. Density-functional theory for plutonium. *Adv. Phys.* **2019**, *68*, 1–47. [CrossRef]
85. Eriksson, O.; Brooks, M.S.S.; Johansson, B. Orbital polarization in narrow-band systems: Application to volume collapses in light lanthanides. *Phys. Rev. B* **1990**, *41*, 7311(R). [CrossRef]
86. Eschrig, H.; Sargolzaei, M.; Koepernik, K.; Richter, M. Orbital polarization in the Kohn-Sham-Dirac theory. *EPL* **2005**, *72*, 611–617. [CrossRef]
87. Kresse, G.; Furthmüller, J. Efficient iterative schemes for ab initio total-energy calculations using a plane-wave basis set. *Phys. Rev. B* **1996**, *54*, 11169–11186. [CrossRef]
88. Kresse, G.; Joubert, D. From ultrasoft pseudopotentials to the projector augmented-wave method. *Phys. Rev. B* **1999**, *59*, 1758–1775. [CrossRef]
89. Saunders, N.; Miodownik, A. *CALPHAD Calculation of Phase Diagrams: A Comprehensive Guide*; Elsevier Science: Amsterdam, The Netherlands, 1998.
90. Lukas, H.; Fries, S.; Sundman, B. *Computational Thermodynamics: The CALPHAD Method*; Cambridge University Press: Cambridge, UK, 2007.

91. Andersson, J.O.; Helander, T.; Höglund, L.; Shi, P.F.; Sundman, B. Thermo-Calc & DICTRA, computational tools for material science. *Calphad* **2002**, *26*, 273–312.

92. Thermo-Calc Software PURE5/Pure Substances Database Version 5. Available online: https://thermocalc.com/products/databases/general-alloys-and-pure-substances/ (accessed on 3 February 2023).

93. Dinsdale, A.T. SGTE data for pure elements. *Calphad* **1991**, *15*, 317–425. [CrossRef]

94. Wilson, A.S.; Rundle, R.E. The structures of uranium metal. *Acta Cryst.* **1949**, *2*, 126–127. [CrossRef]

95. Crocombette, J.; Jollet, F.; Nga, L.; Petit, T. Plane-wave pseudopotential study of point defects in uranium dioxide. *Phys. Rev. B* **2001**, *64*, 104107. [CrossRef]

96. Shang, S.L.; Saengdeejing, A.; Mei, Z.G.; Kim, D.E.; Zhang, H.; Ganeshan, S.; Wang, Y.; Liu, Z.K. First-principles calculations of pure elements: Equations of state and elastic stiffness constants. *Comp. Mater. Sci.* **2010**, *48*, 813–826. [CrossRef]

97. Shapiro, A.B.; Summers, L.T.; Eckels, D.J.; Sahai, V. *Modeling of Casting Microstructures and Defects*; UCRL-ID-128519; LLNL Internal Report: Livermore, CA, USA, 1997.

98. Rohr, W.G.; Wittenberg, L.J. Density of liquid uranium. *J. Phys. Chem.* **1970**, *74*, 1151–1152. [CrossRef]

99. Moore, G.E.; Kelley, K.K. High-temperature heat contents of uranium, uranium dioxide, and uranium trioxide. *J. Am. Chem. Soc.* **1947**, *69*, 2105–2107. [CrossRef] [PubMed]

100. Ginnings, D.C.; Corruccini, R.J. Heat capacities at high temperatures of uranium, uranium trichloride, and uranium tetrachloride. *J. Res. N. B. S.* **1947**, *39*, 309–316. [CrossRef]

101. Levinson, L.S. Heat content of molten uranium. *J. Chem. Phys.* **1964**, *40*, 3584–3585. [CrossRef]

102. Rand, H.; Kubaschewski, O. *Thermochemical Properties of Uranium Compounds*; Oliver and Boyd; Ltd.: Edinburgh, Scotland; London, UK, 1963; p. 36.

103. Fei, Y.; Saxena, S.K. An equation for the heat capacity of solids. *Geochim. Cosmochim. Acta* **1987**, *51*, 251–254. [CrossRef]

104. Holley, C.E., Jr.; Storms, E.K. *Thermodynamics of Nuclear Materials*; Proc. IAEA.: Vienna, Austria, 1968; p. 411.